ARTICLE

doi:10.1038/nature10238

The crystal structure of a voltage-gated sodium channel

Jian Payandeh[1], Todd Scheuer[1], Ning Zheng[1,2] & William A. Catterall[1]

Voltage-gated sodium (Na_V) channels initiate electrical signalling in excitable cells and are the molecular targets for drugs and disease mutations, but the structural basis for their voltage-dependent activation, ion selectivity and drug block is unknown. Here we report the crystal structure of a voltage-gated Na^+ channel from *Arcobacter butzleri* (NavAb) captured in a closed-pore conformation with four activated voltage sensors at 2.7 Å resolution. The arginine gating charges make multiple hydrophilic interactions within the voltage sensor, including unanticipated hydrogen bonds to the protein backbone. Comparisons to previous open-pore potassium channel structures indicate that the voltage-sensor domains and the S4–S5 linkers dilate the central pore by pivoting together around a hinge at the base of the pore module. The NavAb selectivity filter is short, ~4.6 Å wide, and water filled, with four acidic side chains surrounding the narrowest part of the ion conduction pathway. This unique structure presents a high-field-strength anionic coordination site, which confers Na^+ selectivity through partial dehydration via direct interaction with glutamate side chains. Fenestrations in the sides of the pore module are unexpectedly penetrated by fatty acyl chains that extend into the central cavity, and these portals are large enough for the entry of small, hydrophobic pore-blocking drugs. This structure provides the template for understanding electrical signalling in excitable cells and the actions of drugs used for pain, epilepsy and cardiac arrhythmia at the atomic level.

Electrical signals (termed action potentials) encode and process information within the nervous system and regulate a wide range of physiological processes[1,2]. The voltage-gated ion channels (VGICs) that mediate electrical signalling have distinct functional roles[1,2]. Na_V channels initiate action potentials. Voltage-gated calcium (Ca_V) channels initiate processes such as synaptic transmission, muscle contraction and hormone secretion in response to membrane depolarization. Voltage-gated potassium (K_V) channels terminate action potentials and return the membrane potential to its resting value. Na_V channels are mutated in inherited epilepsy, migraine, periodic paralysis, cardiac arrhythmia and chronic pain syndromes[3]. These channels are molecular targets of drugs used in local anaesthesia and in the treatment of genetic and sporadic Na_V channelopathies in the brain, skeletal muscle and heart[4]. The rapid activation, Na^+ selectivity and drug sensitivity of Na_V channels are unique among VGICs[2].

VGICs share a conserved architecture in which four subunits or homologous domains create a central ion-conducting pore surrounded by four voltage sensors[5]. The voltage-sensing domain (VSD) is composed of the S1–S4 segments, and the pore module is formed by the S5 and S6 segments with a P-loop between them[5]. The S4 segments place charged amino acids within the membrane electric field that undergo outward displacement in response to depolarization and initiate opening of the central pore[6,7]. Although the architecture of K_V channels has been established at high resolution[8,9], the structural basis for rapid, voltage-dependent activation of VGICs remains uncertain[7,9], and the structures responsible for Na^+-selective conductance and drug block in Na_V channels are unknown. The primary pore-forming subunits of Na_V and Ca_V proteins in vertebrates are composed of approximately 2,000 amino acid residues in four linked homologous domains[5]. The bacterial NaChBac channel family is an important model for structure–function studies of more complex vertebrate Na_V and Ca_V channels[10,11]. NaChBac is a homotetramer, and its pharmacological profile is similar to Na_V and Ca_V channels[10,12]. Bacterial Na_V channels are highly Na^+ selective, but they can be converted into Ca^{2+}-selective forms through simple mutagenesis[13]. The NaChBac family represents the probable ancestor of vertebrate Na_V and Ca_V channels. Through analysis of the three-dimensional structure of NavAb from *A. butzleri*, we provide the first insights into the structural basis of voltage-dependent gating, ion selectivity and drug block in Na_V and Ca_V channels.

Structure of NavAb in a membrane environment

NavAb is a member of the NaChBac family and functions as a voltage-gated sodium-selective ion channel (Supplementary Figs 1 and 2). Vertebrate Ca_V channels require solubilization in digitonin and Na_V channels require specific lipids to retain function when purified[14,15]. Accordingly, we solubilized NavAb in digitonin, crystallized it in a lipid-based bicelle system, and determined its structure at 2.70 Å resolution (Supplementary Figs 3–6 and Supplementary Table 1). NavAb crystallized as a dimer-of-dimers with 28 lipid molecules bound per tetramer (Supplementary Figs 3 and 6b). Crystal packing indicates a membrane-like environment (Supplementary Fig. 6a). NavAb VSDs interact noncovalently with the pore module of a neighbouring subunit (Fig. 1a), and crystallographic temperature factors highlight their dynamic nature (Supplementary Fig. 6c).

Structure of the activated voltage sensor

S4 segments in VSDs consist of repeated motifs of a positively charged residue, usually arginine, followed by two hydrophobic residues[5–7]. The R2 and R3 'gating charges' in NavAb are positioned to interact with a conserved extracellular negative-charge cluster (ENC; Fig. 1b), whereas the R4 gating charge interacts with a conserved intracellular negative-charge cluster (INC; Fig. 1b). These structural features, in conjunction with disulphide-locking experiments[16,17], indicate that the VSDs are in an activated conformation. These ion-pair interactions are expected to stabilize and catalyse S4 movement in the membrane electric field[7,18,19].

[1]Department of Pharmacology, University of Washington, Seattle, Washington 98195, USA. [2]Howard Hughes Medical Institute, University of Washington, Seattle, Washington 98195, USA.

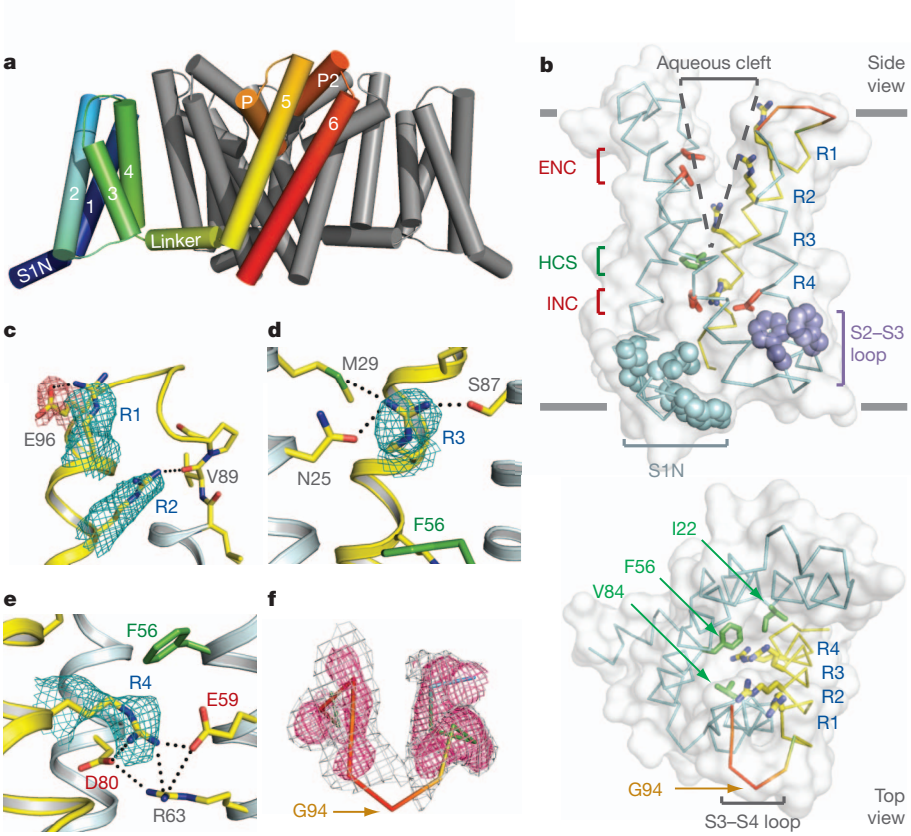

Figure 1 | Structure of NavAb and the activated VSD. a, Structural elements in NavAb. One subunit is highlighted (1–6, transmembrane segments S1–S6). The nearest VSD has been removed for clarity. **b**, Side and top views of the VSD illustrating the ENC (red), INC (red), HCS (green), residues of the S1N helix (cyan) and phenylalanines of the S2–S3 loop (purple). S4 segment and gating charges (R1–R4) are in yellow. **c**–**e**, Hydrogen bonding of gating charges, dotted lines (<3.5 Å). $F_o - F_c$ omit maps are contoured over E96 and R1–R4 at 1, 1, 1.5, 2.5 and 1.75σ, respectively. **f**, S3–S4 loop. Coloured according to crystallographic temperature factors of the main chain (blue <50 Å^2 to red >150 Å^2). An $F_o - F_c$ omit map is contoured at 1.5σ (grey) and 2.5σ (pink).

Highly conserved Arg 63 in the S2 segment also interacts with R4 and the INC (Fig. 1e), which may stabilize the INC and modulate its electrostatics[20]. NavAb has a spectrum of additional gating charge interactions. R1 interacts with Glu 96, R2 forms a hydrogen bond with the backbone carbonyl of Val 89 in S3, and R3 forms hydrogen bonds with Asn 25 and Met 29 in S1, and Ser 87 in S3 (Fig. 1c–e). This conserved network of hydrogen bonds (Supplementary Fig. 7a) should complement exchange of ion-pair partners and provide a low-energy pathway for S4 movement. The R2–backbone interaction would escape detection in mutagenesis experiments (Fig. 1c) and could have unrecognized significance in the passage of gating charges through the gating pore (Fig. 1b).

The S4 segment in NavAb forms a 3_{10}-helix from R1 to R4. This conformation places all four gating charges in a straight line on one side of S4 (Fig. 1b), such that they could move linearly through the central portion of the gating pore, rather than with a spiral motion[7,17–19]. The S3 segment is a straight α-helix, and the S3–S4 loop has a dynamic connection to S4 (Fig. 1f). The lack of structural rigidity within the S3–S4 loop (Fig. 1f) indicates that it could move relatively freely in response to large S4 movements during gating.

Our structural analysis reveals further that the S1N helix and S2–S3 loop shield the intracellular surface of the VSD (Fig. 1b and Supplementary Fig. 8). The S2–S3 loop is conserved among VGICs, and two prominent Phe side chains probably stabilize the VSD in the membrane during gating transitions (Fig. 1b and Supplementary Figs 7 and 8)[9]. The S1N-to-S3 region may behave as a modular unit during activation. In contrast to the sheltered intracellular surface of the VSD, a large aqueous cleft extends ~10 Å from the extracellular surface into the membrane region above the hydrophobic constriction site (HCS; Fig. 1b). The HCS contains highly conserved residues (Ile 22, Phe 56 and Val 84; Supplementary Fig. 7) that seal the VSD against ion leakage during S4 movement (Fig. 1b). The NavAb VSD therefore illustrates two important concepts from structure–function studies of Na_V channels: a large external vestibule accessible to hydrophilic reagents; and a focused membrane electric field over the intracellular half of the VSD[6,7].

Despite their separation over one billion years of evolution, the VSDs of NavAb and $K_V1.2$ show highly similar conformations (Supplementary Fig. 8a). R4 of NavAb is in an equivalent position to K5 in $K_V1.2$ (Supplementary Fig. 8a), the most outward location of K5 during voltage-sensor activation[20]. This observation implies that the NavAb and $K_V1.2$ VSDs are both activated.

The NavAb activation gate is closed

The pore of NavAb is closed, providing the first view of a closed pore in a VGIC (Fig. 2a and Supplementary Fig. 3). Met 221 completely occludes the ion conduction pathway (Supplementary Fig. 4c). The S6 helices of NavAb superimpose well with other closed-pore structures and are distinct from the open-pore $K_V1.2$ structure (Fig. 2a, b). A subtle iris-like dilation of the activation gate may be sufficient to open the pore, and the surrounding cuff of S4–S5 linkers may prevent larger pore opening (Fig. 2a–c).

It is surprising to have a closed pore in a VGIC with activated voltage sensors at 0 mV. Our NavAb structures were obtained by introducing a Cys at two locations near the intracellular end of S6 (Ile217Cys or Met221Cys). Evidently, these substitutions allowed us to trap the NavAb channel in the pre-open state previously invoked in kinetic models of VGIC gating (Supplementary Discussion)[21–23].

Architecture of the pore and selectivity filter

VGICs are selective for specific cations yet conduct these ions at nearly the rate of free diffusion[2]. Our NavAb structure uncovers a

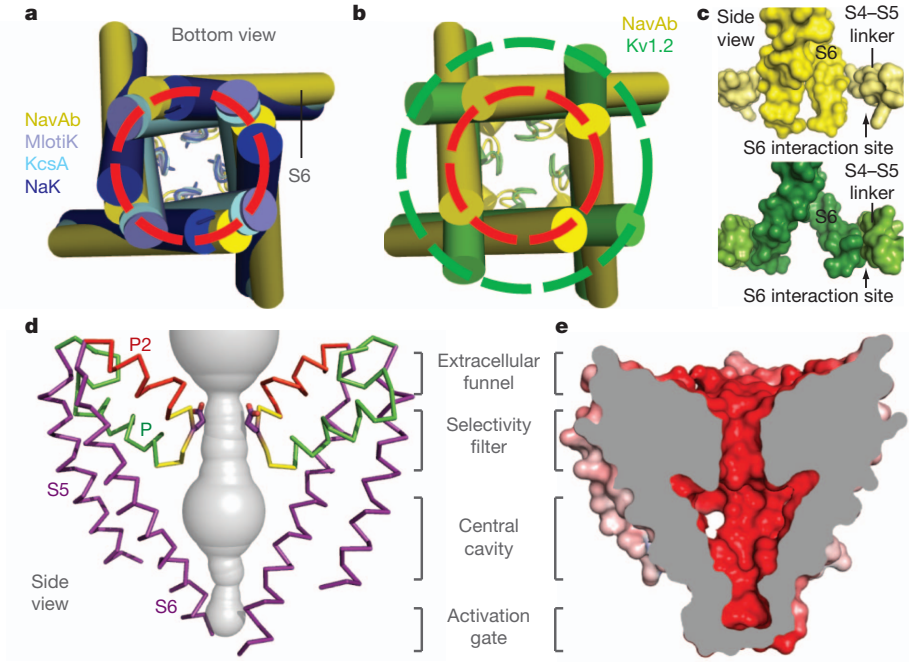

Figure 2 | NavAb pore module. **a**, Pore-lining S6 helices of NavAb (yellow) and the closed MlotiK (PDB code 3BEH), KcsA (PDB code 1K4C) and NaK (PDB code 2AHY) channels. Cα locations of Met 221 define a common radius for the closed activation gate (red circle). **b**, Comparison of S6 helices of NavAb and $K_V1.2/2.1$ (PDB code 2R9R). Dashed circle in red indicates radius of Cα atoms of Met 221 in NavAb. **c**, Site for interaction of S6 with S4–S5 linkers (top, NavAb; bottom, $K_V1.2/2.1$). **d**, Architecture of the NavAb pore. Glu 177 side chains (purple sticks); pore volume is shown in grey. **e**, Electrostatic potential coloured from −10 to 10 kT (red to blue).

basis for the selectivity and high conductance of Na_V channels. The NavAb pore module consists of an outer funnel-like vestibule, a selectivity filter, a central cavity and an intracellular activation gate (Fig. 2d and Supplementary Fig. 4b). The large central cavity in NavAb could easily accommodate a Na^+ ion with its first hydration shell and would present a hydrophobic surface over which ions should rapidly diffuse (Fig. 2e and Supplementary Figs 1 and 9). The pore (P)-helices are positioned to stabilize cations in the central cavity through helical–dipole interactions (Fig. 2d and Supplementary Fig. 4b), as suggested for K^+ channels[24,25]. Notably, a second pore-helix (P2-helix) forms an extracellular funnel in NavAb (Fig. 2d). This unique P2-helix is not seen in K^+ channels and may represent a conserved structural element in the outer vestibule of Na_V and Ca_V channels.

The ion conduction pathway in NavAb is strongly electronegative and the selectivity filter forms the narrowest constriction near the extracellular side of the membrane (Figs 2d, e, 3 and Supplementary Fig. 9). Classic permeation studies suggested a high-field-strength anionic site with dimensions of ~3.1 × 5.1 Å for the selectivity filter in Na_V channels[26,27] and 5.5 × 5.5 Å in Ca_V channels[28]. Mutagenesis studies implicated Glu side chains as key determinants of ion selectivity in these channels[29–33]. In NavAb, the four Glu 177 side chains form a ~6.5 × 6.5 Å scaffold with an orifice of ~4.6 × 4.6 Å defined by van der Waals surfaces (Fig. 3a and Supplementary Fig. 9d). Remarkably, Glu 177 aligns with Glu residues that determine ion selectivity in Na_V and Ca_V channels (Fig. 3e).

The Glu 177 side chains of NavAb are supported by an elaborate architecture (Supplementary Figs 10 and 11). The P-helix ends with the conserved Thr 175, which accepts a hydrogen bond (3.0 Å) from the conserved Trp 179 of a neighbouring subunit (Fig. 3a). This landmark interaction staples together adjacent subunits at the selectivity filter. The residues between Thr 175 and Trp 179 form a tight turn and expose backbone carbonyls of Thr 175 and Leu 176 to conducted ions (Fig. 3b). The Glu 177 side chains form hydrogen bonds with the backbone amides of Ser 180 (2.6 Å) and Met 181 (3.1 Å) from the P2-helix (Fig. 3b and Supplementary Fig. 10). An extensive network of additional interactions (Supplementary Fig. 10), including hydrogen bonds between Gln 172 from the P-helix and the carbonyl of Glu 177 (Fig. 3a, b), further stabilizes the selectivity filter. Owing to the dimer-of-dimers arrangement, the Glu 177 and Ser 178 side chains of NavAb are in two slightly different environments (Fig. 3a and Supplementary Fig. 11), consistent with functional nonequivalence of the corresponding glutamates in Ca_V channels[31–33].

In agreement with the low affinity of Na_V channels for permeant ions (K_d for $Na^+ > 350$ mM[34]), no extra density was observed beside the Glu 177 side chains. Instead, strong electron densities were found above Glu 177 at a distance of >4 Å. These densities probably represent cations or solvent molecules (Ion_{EX}; Fig. 3b) positioned above the selectivity filter by its intense electronegativity (Fig. 2e).

Ion permeation and selectivity

NavAb represents a prototype for understanding Na^+ selectivity and permeation. Analysis of the pore radius indicates that a partially hydrated Na^+ ion can be accommodated at the high-field-strength site formed by the Glu 177 side chains ($Site_{HFS}$; Fig. 3a, b and Supplementary Fig. 9d). The much narrower K^+-channel filter can fit inside the NavAb selectivity filter (Fig. 3c). Careful inspection of the electron density indicates four well-bound water molecules 2.5 Å from the Leu 176 carbonyls ($Site_{CEN}$; Fig. 3b). Remarkably, these four water molecules occupy the same positions as the site 3 carbonyls from K^+ channels (Fig. 3c, d)[35]. A distance of 2.5 Å is also found between the backbone carbonyls of Thr 175 from NavAb and the site 4 carbonyls of K^+ channels (Fig. 3c, d)[35]. Analogous to other Na^+ complexes (Supplementary Fig. 12)[36–40], a Na^+ ion surrounded by a square array of four water molecules could interact with the backbone carbonyls of Leu 176 ($Site_{CEN}$) or Thr 175 ($Site_{IN}$) (Fig. 3d and Supplementary Fig. 12). Therefore, unlike K^+ channels, the NavAb selectivity filter seems to select and conduct Na^+ ions in a mostly hydrated form.

The NavAb structure fits closely with Hille's single-ion pore model for Na_V channels, in which a high-field-strength anion partially dehydrates the permeating ion[2,34]. According to Eisenman's theory[41], a Na^+ ion would approach the $Site_{HFS}$ more closely than the larger

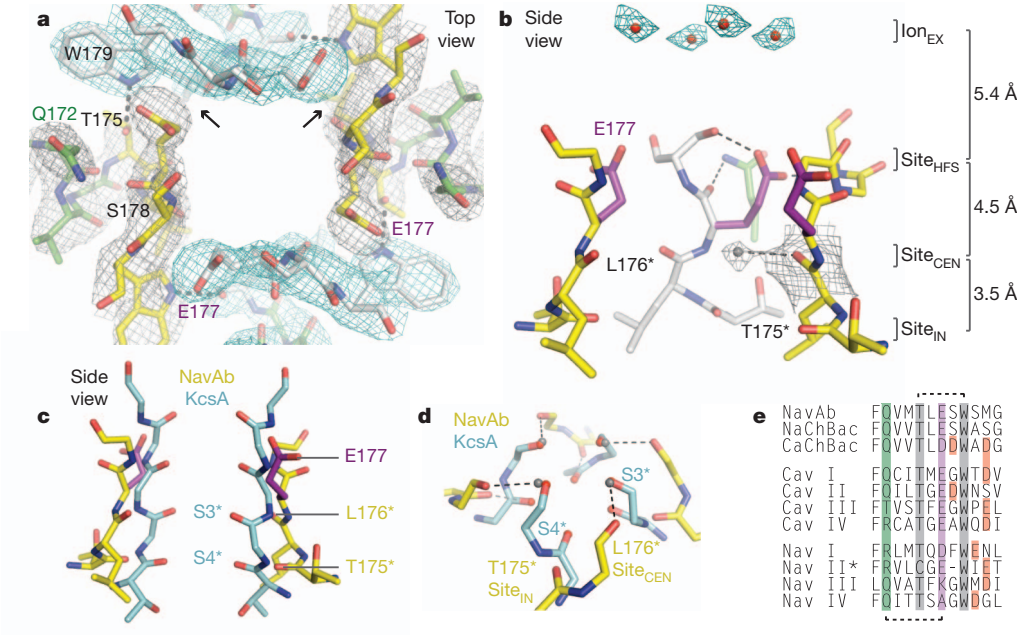

Figure 3 | Structure of the NavAb selectivity filter. **a**, Top view of the selectivity filter. Symmetry-related molecules are coloured white and yellow; P-helix residues are coloured green. Hydrogen bonds between Thr 175 and Trp 179 are indicated by grey dashes. Electron densities from $F_o - F_c$ omit maps are contoured at 4.0σ (blue and grey) and subtle differences can be appreciated (small arrows). **b**, Side view of the selectivity filter. Glu 177 (purple) interactions with Gln 172, Ser 178 and the backbone of Ser 180 are shown in the far subunit. $F_o - F_c$ omit map, 4.75σ (blue); putative cations or water molecules (red spheres, Ion_{EX}). Electron density around Leu 176 (grey; $F_o - F_c$ omit map at 1.75σ) and a putative water molecule is shown (grey sphere). Na^+-coordination sites: $Site_{HFS}$, $Site_{CEN}$ and $Site_{IN}$. **c**, Superposition of NavAb and a K^+-channel selectivity filter. NavAb Glu 177 side chains are shown in purple, backbone carbonyls are indicated with an asterisk; the K^+ channel is shown in blue (PDB code 1K4C), site 3 and site 4 backbone carbonyls[35] are indicated with an asterisk. This structural alignment is based on P-helices. **d**, Enlarged view of $Site_{CEN}$ and $Site_{IN}$. Putative water molecules are shown as grey spheres; dotted lines, ~2.5 Å. **e**, Selectivity filter sequence alignment. E177 homologues are shaded purple; outer ring of negatively charged residues is shaded orange.

K^+ ion, allowing more efficient removal of water and faster permeation (Fig. 3a, b)[34]. A Na^+ ion could fit in-plane between the Glu 177 side chains, with one side chain coordinating the Na^+ ion directly and neighbouring Glu 177 side chains acting as hydrogen bond acceptors for two in-plane water molecules[26,27,34]. With two additional waters remaining axial to the ion, this arrangement would approximate trigonal bipyramidal coordination[38]. Because only one Glu 177 side chain engages the permeating ion directly, this transient complex would be inherently asymmetric. When the permeating ion escapes $Site_{HFS}$, full rehydration would occur along the water-lined sites formed by the backbone carbonyls of Leu 176 ($Site_{CEN}$) and Thr 175 ($Site_{IN}$; Fig. 3b, d and Supplementary Fig. 12). Free diffusion then allows the hydrated Na^+ ion to enter the central cavity and move through the open activation gate into the cytoplasm[34]. The selectivity-filter structure of NavAb concentrates barriers to ion flow into ~5 Å (Fig. 3b and Supplementary Fig. 9d), which should promote high flux rates[34]. This permeation mechanism probably reflects the high free energy of Na^+ hydration, where further removal of solvating waters would present too high an energy barrier. In sharp contrast, K^+-selective channels conduct nearly fully dehydrated K^+ ions through direct interactions with backbone carbonyls in a long, narrow, multi-ion pore[35,36]. The architectures of the selectivity filters of vertebrate Na_V and Ca_V channels probably resemble NavAb, and amino acid substitutions within this structural framework must impart Na^+ versus Ca^{2+} selectivity (Supplementary Discussion)[13,29–33].

Interaction sites of pore blockers

NavAb provides a foundation to interpret pharmacological mechanisms. From the extracellular side, the Glu 177 side chains of NavAb represent the blocking site in Na_V channels for protons and guanidinium moieties of tetrodotoxin and saxitoxin[2,42], as well as the site where divalent cations and protons bind and block Ca_V channels (Fig. 3)[31–33]. From the intracellular side, local anaesthetics, antiarrhythmics and antiepileptic drugs block Na_V and Ca_V channels[2,4] by entering through the open intracellular mouth of the pore and binding to an overlapping receptor site on the S6 segments[43–45]. Alignment of NavAb S6 segments with vertebrate Na_V and Ca_V channels reveals a high degree of sequence similarity (Supplementary Fig. 7b), and drug molecules could easily fit into the large central cavity (Fig. 2e and Supplementary Fig. 9). Use-dependent block is enhanced by repetitive opening of the pore to provide drug access[2,46], and the local anaesthetic etidocaine is an open-channel blocker of NaChBac[12]. The tight seal observed at the intracellular activation gate in NavAb illustrates why pore opening is required for access of large or hydrophilic drugs to the S6 receptor site (Fig. 2 and Supplementary Fig. 4c).

Fenestrations provide hydrophobic access to pore

Membrane lipids modulate the structure and function of VGICs[8,9,47,48]. However, NavAb presents a completely unexpected type of lipid interaction that has profound implications. The NavAb central cavity reveals four lateral openings leading from the membrane to the lumen of the closed pore (Fig. 4). These fenestrations measure ~8 × 10 Å, and could become larger depending upon nearby side-chain conformations (Phe 203; Fig. 4). Lipids penetrate through these side portals and lie deep within the central cavity, occluding the ion conduction pathway in NavAb (Fig. 4, red). Because acyl-chain-containing detergents were never used in the preparation of NavAb crystals, these electron densities are assigned as acyl chains of membrane phospholipids. Similar fenestrations were not observed in the open-pore structure of $K_V1.2$ (refs 8, 9), raising the possibility that these lipid chains withdraw and the fenestrations close in the open state.

The lateral pore fenestrations in NavAb lead directly to the drug-binding sites within the central cavity and abut residues that are important for drug binding in Na_V and Ca_V channels (Fig. 4 and Supplementary Fig. 7b)[43,44]. These NavAb portals appear compatible

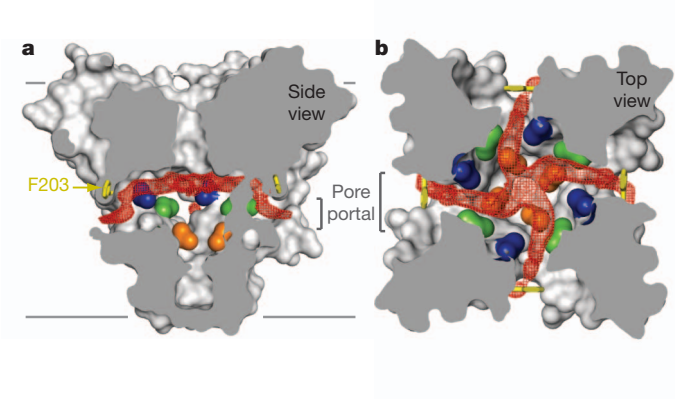

Figure 4 | Membrane access to the central cavity in NavAb. **a**, Side view through the pore module illustrating fenestrations (portals) and hydrophobic access to central cavity. Phe 203 side chains are shown as yellow sticks. Surface representations of NavAb residues aligning with those implicated in drug binding and block: Thr 206, blue; Met 209, green; Val 213, orange. Membrane boundaries, grey lines. Electron density from an $F_o - F_c$ omit map is contoured at 2.0σ. **b**, Top view sectioned below the selectivity filter, coloured as in **a**.

with the passage of small neutral or hydrophobic drugs such as phenytoin[49] and benzocaine[46], which can gain access to their receptor site in closed channels[2,46]. We propose that pore fenestrations may be directly involved in voltage-dependent drug block according to the 'modulated receptor model'[46]. Our findings highlight the potential for lipids and other hydrophobic molecules to influence the function of ion channels from the lipid phase of the membrane.

Structural basis for central pore gating

The domain-swapped arrangement of the VSD around the pore allows the S4–S5 linker to couple S4 movements to activation of VGICs (Fig. 1a)[9]. Kinetic models indicate that all four voltage sensors activate and then the central pore opens in a concerted transition[21–23]. An essential element of this gating model is a state in which all four VSDs have activated but the pore remains closed[21–23]. It is likely that we have captured this pre-open state in our crystals (Supplementary Discussion). NavAb therefore provides a unique opportunity to consider the structural basis for coupling of VSD activation to pore opening.

When activated VSDs of NavAb and $K_V1.2$ are overlaid (Supplementary Fig. 8a), the S4–S5 linkers superimpose precisely, but the pore domains diverge at the foot of S5 (Fig. 5a). Superposition of the pore domains demonstrates an equivalent displacement of the VSDs (Supplementary Fig. 13). These comparisons lead to a working model for pore opening. First, during activation, the S4–S5 linker and VSD move together as a modular unit (Fig. 5a). Second, a single molecular hinge at the base of S5 mediates the closed-to-open pore transition (Fig. 5a, b). Third, tight structural coupling is maintained between the S5 and S6 segments (Supplementary Fig. 13a). This model suggests that rotation of the VSD and S4–S5 linker as a structural unit pulls the S5–S6 helices outward to open the pore (Fig. 5b and Supplementary Fig. 13b). Because of their tight structural coupling, displacement of the S5–S6 segments from one subunit forces the neighbouring subunits to move similarly, leading to concerted pore opening. During this transition, the amphipathic S4–S5 linker pivots along the plane of the membrane interface (Fig. 5b and Supplementary Figs 7 and 13b). In contrast to $K_V1.2$, the S6 helices in NavAb have not fully engaged their interaction site on the S4–S5 linker (Fig. 2c), in agreement with the pre-open state of NavAb. A rolling motion of the VSDs around the pore produces displacements up to ~10 Å at the intracellular side (Fig. 5b and Supplementary Fig. 13b), which may influence movements of the S1N helix and the conserved S2–S3 loop.

In NavAb, a 3_{10}-helix extends from R1 to R4 (Fig. 1b). In $K_V1.2$, a 3_{10}-helix encompasses R3 to K5 (equivalent to NavAb R2 to R4), but

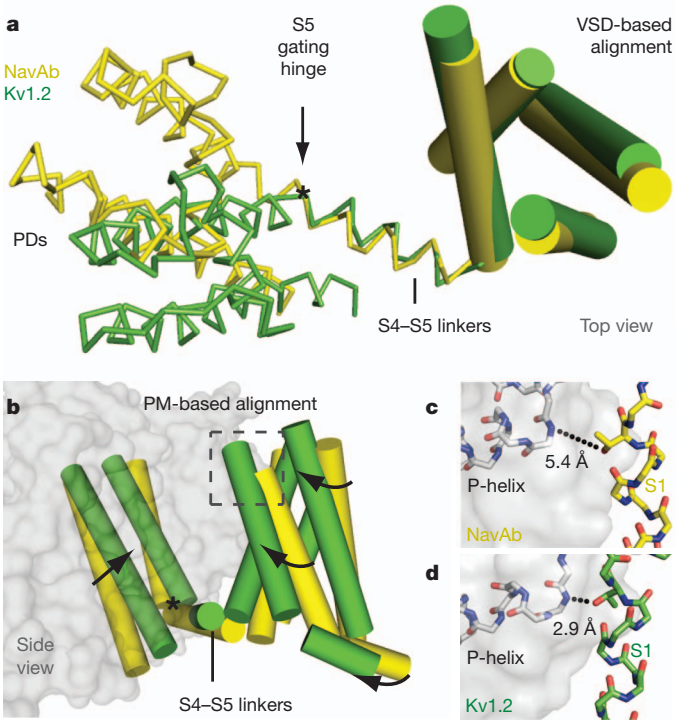

Figure 5 | Model for activation gate opening. **a**, Superposition of NavAb and $K_V1.2/2.1$ on the basis of their VSDs (cylinders). PDs, pore domains. **b**, Superposition of NavAb and $K_V1.2/2.1$ tetrameric pore modules (PM) viewed from the membrane. S5 gating hinge is indicated with an asterisk. Dashed square is enlarged in panels **c** and **d**. **c**, **d**, S1 interaction with P-helix. The distance from the S1 Thr to the P-helix of the neighbouring subunit is 2.9 Å in $K_V1.2/2.1$, but >4.5 Å in NavAb.

the remaining S4 segment is α-helical[9]. Conceivably, energy derived from voltage-driven translocation of S4 may be stored in the higher-energy 3_{10}-helix, and then released to help drive pore opening. The VSDs in $K_V1.2$ are displaced outward (~2 Å) compared to the pre-open NavAb structure (Fig. 5b), which could account for the small gating current associated with concerted pore opening[6]. At the extracellular side of the VSD, an S1 threonine residue hydrogen bonds (2.9 Å) with the P-helix of a neighbouring subunit in $K_V1.2$ (Fig. 5d), providing a conserved contact point that allows the VSD to perform mechanical work on the pore[50]. The equivalent S1 threonine in NavAb has not yet engaged the P-helix (Fig. 5c). This interaction may therefore represent an essential step in activation gating that has not yet occurred in the pre-open state of NavAb.

Conclusion

The structure of NavAb provides key insights into the molecular basis of voltage sensing, ion conductance and voltage-dependent gating in a historic class of ion channels[1,2]. A new network of interactions within the VSD appears well positioned to catalyse gating charge movements during activation. Our model for electromechanical coupling reveals a rolling motion of the VSD and its connecting S4–S5 linker around the pore. The NavAb selectivity filter illustrates the basis for selective Na^+ conductance through a water-lined pore featuring a high-field-strength anionic site. Lastly, hydrophobic access from the membrane phase has been uncovered as a potentially important pathway for drug binding and modulation of VGICs.

METHODS SUMMARY

NavAb was expressed in insect cells and purified using anti-Flag resin and size-exclusion chromatography, reconstituted into DMPC:CHAPSO bicelles, and crystallized over an ammonium sulphate solution containing 0.1 M Na-citrate,

pH 4.75. Cysteine mutants were complexed with mercury to obtain initial experimental phases. A single anomalous dispersion (SAD) data set from a mercury-free SeMet-substituted protein crystal expedited model building. Standard crystallographic refinement procedures and structural analyses were performed. Electrophysiological experiments on NavAb were performed in tsA-201 cells using standard protocols.

Full Methods and any associated references are available in the online version of the paper at www.nature.com/nature.

Received 16 January; accepted 27 May 2011.

Published online 10 July; corrected 21 July 2011 (see full-text HTML version for details).

1. Hodgkin, A. L. & Huxley, A. F. A quantitative description of membrane current and its application to conduction and excitation in nerve. *J. Physiol. (Lond.)* **117,** 500–544 (1952).
2. Hille, B. *Ion Channels of Excitable Membranes* 3rd edn (Sinauer Associates, 2001).
3. Ryan, D. P. & Ptacek, L. J. Episodic neurological channelopathies. *Neuron* **68,** 282–292 (2010).
4. Catterall, W. A. Common modes of drug action on Na^+ channels: local anesthetics, antiarrhythmics and anticonvulsants. *Trends Pharmacol. Sci.* **8,** 57–65 (1987).
5. Yu, F. H. & Catterall, W. A. The VGL-chanome: a protein superfamily specialized for electrical signaling and ionic homeostasis. *Sci. STKE* **2004,** re15 (2004).
6. Bezanilla, F. The action potential: from voltage-gated conductances to molecular structures. *Biol. Res.* **39,** 425–435 (2006).
7. Catterall, W. A. Ion channel voltage sensors: structure, function, and pathophysiology. *Neuron* **67,** 915–928 (2010).
8. Long, S. B., Campbell, E. B. & Mackinnon, R. Crystal structure of a mammalian voltage-dependent Shaker family K^+ channel. *Science* **309,** 897–903 (2005).
9. Long, S. B., Tao, X., Campbell, E. B. & MacKinnon, R. Atomic structure of a voltage-dependent K^+ channel in a lipid membrane-like environment. *Nature* **450,** 376–382 (2007).
10. Ren, D. *et al.* A prokaryotic voltage-gated sodium channel. *Science* **294,** 2372–2375 (2001).
11. Koishi, R. *et al.* A superfamily of voltage-gated sodium channels in bacteria. *J. Biol. Chem.* **279,** 9532–9538 (2004).
12. Zhao, Y., Scheuer, T. & Catterall, W. A. Reversed voltage-dependent gating of a bacterial sodium channel with proline substitutions in the S6 transmembrane segment. *Proc. Natl Acad. Sci. USA* **101,** 17873–17878 (2004).
13. Yue, L., Navarro, B., Ren, D., Ramos, A. & Clapham, D. E. The cation selectivity filter of the bacterial sodium channel, NaChBac. *J. Gen. Physiol.* **120,** 845–853 (2002).
14. Curtis, B. M. & Catterall, W. A. Reconstitution of the voltage-sensitive calcium channel purified from skeletal muscle transverse tubules. *Biochemistry* **25,** 3077–3083 (1986).
15. Feller, D. J., Talvenheimo, J. A. & Catterall, W. A. The sodium channel from rat brain. Reconstitution of voltage-dependent scorpion toxin binding in vesicles of defined lipid composition. *J. Biol. Chem.* **260,** 11542–11547 (1985).
16. DeCaen, P. G., Yarov-Yarovoy, V., Zhao, Y., Scheuer, T. & Catterall, W. A. Disulfide locking a sodium channel voltage sensor reveals ion pair formation during activation. *Proc. Natl Acad. Sci. USA* **105,** 15142–15147 (2008).
17. DeCaen, P. G., Yarov-Yarovoy, V., Sharp, E. M., Scheuer, T. & Catterall, W. A. Sequential formation of ion pairs during activation of a sodium channel voltage sensor. *Proc. Natl Acad. Sci. USA* **106,** 22498–22503 (2009).
18. Catterall, W. A. Molecular properties of voltage-sensitive sodium channels. *Annu. Rev. Biochem.* **55,** 953–985 (1986).
19. Yarov-Yarovoy, V., Baker, D. & Catterall, W. A. Voltage sensor conformations in the open and closed states in ROSETTA structural models of K^+ channels. *Proc. Natl Acad. Sci. USA* **103,** 7292–7297 (2006).
20. Tao, X., Lee, A., Limapichat, W., Dougherty, D. A. & MacKinnon, R. A gating charge transfer center in voltage sensors. *Science* **328,** 67–73 (2010).
21. Zagotta, W. N., Hoshi, T. & Aldrich, R. W. Shaker potassium channel gating. III: Evaluation of kinetic models for activation. *J. Gen. Physiol.* **103,** 321–362 (1994).
22. Kuzmenkin, A., Bezanilla, F. & Correa, A. M. Gating of the bacterial sodium channel, NaChBac: voltage-dependent charge movement and gating currents. *J. Gen. Physiol.* **124,** 349–356 (2004).
23. Zhao, Y., Yarov-Yarovoy, V., Scheuer, T. & Catterall, W. A. A gating hinge in Na^+ channels; a molecular switch for electrical signaling. *Neuron* **41,** 859–865 (2004).
24. Doyle, D. A. *et al.* The structure of the potassium channel: molecular basis of K^+ conduction and selectivity. *Science* **280,** 69–77 (1998).
25. Jogini, V. & Roux, B. Electrostatics of the intracellular vestibule of K^+ channels. *J. Mol. Biol.* **354,** 272–288 (2005).
26. Hille, B. The permeability of the sodium channel to organic cations in myelinated nerve. *J. Gen. Physiol.* **58,** 599–619 (1971).
27. Hille, B. The permeability of the sodium channel to metal cations in myelinated nerve. *J. Gen. Physiol.* **59,** 637–658 (1972).
28. McCleskey, E. W. & Almers, W. The Ca channel in skeletal muscle is a large pore. *Proc. Natl Acad. Sci. USA* **82,** 7149–7153 (1985).
29. Heinemann, S. H., Terlau, H., Stuhmer, W., Imoto, K. & Numa, S. Calcium channel characteristics conferred on the sodium channel by single mutations. *Nature* **356,** 441–443 (1992).
30. Favre, I., Moczydlowski, E. & Schild, L. On the structural basis for ionic selectivity among Na^+, K^+, and Ca^{2+} in the voltage-gated sodium channel. *Biophys. J.* **71,** 3110–3125 (1996).
31. Yang, J., Ellinor, P. T., Sather, W. A., Zhang, J. F. & Tsien, R. W. Molecular determinants of Ca^{2+} selectivity and ion permeation in L-type Ca^{2+} channels. *Nature* **366,** 158–161 (1993).
32. Ellinor, P. T., Yang, J., Sather, W. A., Zhang, J. F. & Tsien, R. W. Ca^{2+} channel selectivity at a single locus for high-affinity Ca^{2+} interactions. *Neuron* **15,** 1121–1132 (1995).
33. Chen, X. H., Bezprozvanny, I. & Tsien, R. W. Molecular basis of proton block of L-type Ca^{2+} channels. *J. Gen. Physiol.* **108,** 363–374 (1996).
34. Hille, B. Ionic selectivity, saturation, and block in sodium channels. A four-barrier model. *J. Gen. Physiol.* **66,** 535–560 (1975).
35. Morais-Cabral, J. H., Zhou, Y. & MacKinnon, R. Energetic optimization of ion conduction rate by the K^+ selectivity filter. *Nature* **414,** 37–42 (2001).
36. Ye, S., Li, Y. & Jiang, Y. Novel insights into K^+ selectivity from high-resolution structures of an open K^+ channel pore. *Nature Struct. Mol. Biol.* **17,** 1019–1023 (2010).
37. Alam, A. & Jiang, Y. Structural analysis of ion selectivity in the NaK channel. *Nature Struct. Mol. Biol.* **16,** 35–41 (2009).
38. Doi, M. *et al.* Caged and clustered structures of endothelin inhibitor BQ123, cyclo(-D-Trp-D-Asp$^-$-Pro-D-Val-Leu-).Na^+, forming five and six coordination bonds between sodium ions and peptides. *Acta Crystallogr. D* **57,** 628–634 (2001).
39. Harding, M. M. Metal-ligand geometry relevant to proteins and in proteins: sodium and potassium. *Acta Crystallogr. D* **58,** 872–874 (2002).
40. Phillips, K., Dauter, Z., Murchie, A. I., Lilley, D. M. & Luisi, B. The crystal structure of a parallel-stranded guanine tetraplex at 0.95 Å resolution. *J. Mol. Biol.* **273,** 171–182 (1997).
41. Eisenman, G. & Horn, R. Ionic selectivity revisited: the role of kinetic and equilibrium processes in ion permeation through channels. *J. Membr. Biol.* **76,** 197–225 (1983).
42. Noda, M., Suzuki, H., Numa, S. & Stuhmer, W. A single point mutation confers tetrodotoxin and saxitoxin insensitivity on the sodium channel II. *FEBS Lett.* **259,** 213–216 (1989).
43. Hockerman, G. H., Peterson, B. Z., Johnson, B. D. & Catterall, W. A. Molecular determinants of drug binding and action on L-type calcium channels. *Annu. Rev. Pharmacol. Toxicol.* **37,** 361–396 (1997).
44. Ragsdale, D. S., McPhee, J. C., Scheuer, T. & Catterall, W. A. Molecular determinants of state-dependent block of Na^+ channels by local anesthetics. *Science* **265,** 1724–1728 (1994).
45. Ragsdale, D. S., McPhee, J. C., Scheuer, T. & Catterall, W. A. Common molecular determinants of local anesthetic, antiarrhythmic, and anticonvulsant block of voltage-gated Na^+ channels. *Proc. Natl Acad. Sci. USA* **93,** 9270–9275 (1996).
46. Hille, B. Local anesthetics: hydrophilic and hydrophobic pathways for the drug-receptor reaction. *J. Gen. Physiol.* **69,** 497–515 (1977).
47. Oliver, D. *et al.* Functional conversion between A-type and delayed rectifier K^+ channels by membrane lipids. *Science* **304,** 265–270 (2004).
48. Delmas, P., Coste, B., Gamper, N. & Shapiro, M. S. Phosphoinositide lipid second messengers: new paradigms for calcium channel modulation. *Neuron* **47,** 179–182 (2005).
49. Morello, R. S., Begenisich, T. & Yeh, J. Z. Determination of the active form of phenytoin. *J. Pharmacol. Exp. Ther.* **230,** 156–161 (1984).
50. Lee, S. Y., Banerjee, A. & MacKinnon, R. Two separate interfaces between the voltage sensor and pore are required for the function of voltage-dependent K^+ channels. *PLoS Biol.* **7,** e47 (2009).

Supplementary Information is linked to the online version of the paper at www.nature.com/nature.

Acknowledgements We thank B. Hille for comments on a draft of the manuscript and members of the N.Z. and W.A.C. groups for their support throughout this project. We are grateful to investigators who provided genomic DNA and the beamline staff at the Advanced Light Source (BL8.2.1 and BL8.2.2) for their assistance during data collection. J.P. acknowledges support from a Canadian Institutes of Health Research fellowship and the encouragement of E. Payandeh. This work was supported by grants from the National Institutes of Health (R01 NS15751 and U01 NS058039 to W.A.C.) and by the Howard Hughes Medical Institute (N.Z.).

Author Contributions N.Z. and W.A.C. are co-senior authors. J.P., N.Z. and W.A.C. conceived and J.P. conducted the protein purification and crystallization experiments. J.P. and N.Z. determined and analysed the structures of NavAb. J.P. and T.S. performed functional studies of NavAb. J.P., N.Z. and W.A.C. wrote the manuscript.

Author Information Coordinates and structure factors have been deposited in the Protein Data Bank under accession codes 3RVY, 3RVZ and 3RW0. Reprints and permissions information is available at www.nature.com/reprints. The authors declare no competing financial interests. Readers are welcome to comment on the online version of this article at www.nature.com/nature. Correspondence and requests for materials should be addressed to N.Z. (nzheng@uw.edu) and W.A.C. (wcatt@uw.edu).

METHODS

Protein expression and purification. After exploring traditional expression approaches in *Escherichia coli*[51], the NavAb channel from *A. butzleri* was cloned into the pFASTBac-Dual vector behind the polyhedron promoter using the BamHI and NotI restriction sites preceded by an N-terminal Flag tag. Recombinant baculovirus were generated using the Bac-to-Bac system (Invitrogen) and insect cells were infected for large-scale protein production. Cells were harvested 72 h post-infection and resuspended in 50 mM Tris pH 8.0, 200 mM NaCl (Buffer A) supplemented with protease inhibitors and DNase. After sonication, digitonin (EMD Biosciences) was added to 1% and solubilization was carried out for 1–2 h at 4 °C. After centrifugation, clarified supernatant was gently agitated with anti-Flag M2-agarose resin (Sigma) pre-equilibrated with Buffer B (Buffer A supplemented with 0.12% digitonin) for 1–2 h at 4 °C. Flag resin was collected in a column by gravity flow, washed with ten column volumes of Buffer B, and eluted with two column volumes of Buffer B supplemented with 0.1 mg ml^{-1} Flag peptide. The eluate was passed over a Superdex 200 column (GE Healthcare) in 10 mM Tris pH 8, 100 mM NaCl and 0.12% digitonin and peak fractions containing NavAb were concentrated using a Vivaspin (30K MWKO) centrifugal device. Site-directed mutagenesis was performed using the standard QuikChange protocol (Stratagene) and all constructs were confirmed by DNA sequencing. Selenomethionine-labelled proteins were expressed using established protocols[52], except cells were washed and starved for methionine at 8 h after infection, followed by SeMet (Anatrace) supplementation at 12 h after infection. SeMet-labelled proteins were purified as described earlier.

Heavy atom screening and labelling. During our efforts to identify useful derivatives for crystallographic phasing, we ultimately turned to the fluorescence detection of heavy atom labelling (FD-HAL) method[53]. Over thirty NavAb single-site cysteine mutations were rapidly screened using the FD-HAL method, and many of these mutant proteins were subsequently crystallized, presumably as covalent mercury-channel complexes. The NavAb(Ile217Cys) and NavAb(Met221Cys) mutants that yielded useful single anomalous dispersion (SAD) data sets were prepared as follows: proteins were purified as described earlier and concentrated to ~1 mg ml^{-1}; $HgCl_2$ was added to a final concentration of 10 mM and the mixture was incubated at room temperature (22 °C) for 2 h. The protein buffer was subsequently exchanged (into mercury-free buffer) through five rounds of concentration and dilution using Vivaspin (30K MWKO) centrifugal devices. Following structure determination, it became apparent that Met 221 lines the narrowest portion of the closed NavAb pore.

NavAb crystallization and data collection. Before crystallization, NavAb was concentrated to ~20 mg ml^{-1} and reconstituted into DMPC:CHAPSO (Anatrace) bicelles according to standard protocols[54,55]. The NavAb-bicelle preparation was mixed in a 1:1 ratio and setup in a hanging-drop vapour-diffusion format over a well solution containing 1.8–2.1 M ammonium sulphate, 100 mM Na-citrate pH 4.75. The mercury-free proteins, the mercury complexes, and the SeMet-labelled proteins all crystallized under essentially identical conditions. Crystals were typically passed through solutions containing 2 M ammonium sulphate, 100 mM Na-citrate pH 4.75 and 28% glucose (wt/v) in increments of ~6% glucose during harvesting. Crystals were plunged into liquid nitrogen and maintained at 100 K during all data collection procedures.

Over 1,000 crystals were screened and nearly 100 diffraction data sets were collected at a synchrotron radiation source (Advanced Light Source, BL8.2.1 and BL8.2.2). A SAD data set collected near the mercury absorption edge ($\lambda = 1.005$ Å) from a mercury-containing complex of the NavAb(Ile217Cys) mutant was ultimately used to determine initial experimental phases. Our highest resolution SeMet SAD data set was collected near the selenium absorption edge ($\lambda = 0.9795$ Å) from a mercury-free NavAb(Met221Cys) SeMet-labelled crystal. Subsequent native (that is, mercury-free) data sets were collected at standard wavelengths. Because the NavAb crystals were small (typically <0.15 mm $\times$ 0.15 mm $\times$ 0.15 mm), contained a high solvent content (~80%), were weakly diffracting, and radiation sensitive, special care was taken to minimize exposure times and to orient the crystals in order to maximize data completeness and quality.

Structure determination and refinement. X-ray diffraction data were integrated and scaled with the HKL2000 suite or DENZO/SCALEPACK[56] and, when required, further processed with the CCP4 package[57]. Experimental phases were determined using a 3.4 Å SAD data set from a Hg-containing NavAb(Ile217Cys) crystal. The SOLVE/RESOLVE[58] software were run in a standard setting and the first map, calculated at 3.7 Å, is shown in Supplementary Fig. 3. Ideal poly-alanine α-helices were manually fitted into this map and the model was subsequently used in combined SAD-molecular replacement (MR) protocols within the Phenix software[59] using a 3.3 Å SAD data set obtained from a SeMet-labelled NavAb(Met221Cys) crystal. SAD-MR and MR-SAD-based maps were calculated and compared, allowing for complete register and amino acid assignment of the NavAb model. Higher-resolution native data sets were ultimately obtained and phased by MR methods using the CNS suite[60] (although our best native NavAb(Met221Cys) data set is actually from a SeMet-containing crystal). Reiterative rounds of model building in O[61] were guided by inspection of omit maps and refinement with CNS[60] was performed with strict NCS-restraints, which were later relaxed during final rounds of refinement. Two strong densities (one per protein chain) assigned as solvent molecules (near the pore turret loop; not discussed in the main text) and all lipid molecules were added to the models at very late stages of refinement. Although trace amounts of digitonin are present in the crystallization condition, digitonin molecules were not readily observed in any electron density map. Refinement statistics, scaling statistics, and overall map quality were ultimately used to assign the NavAb space group as *I*222, although the data were found to closely mimic *I*422 (R_{work}/R_{free} stall at ~32% in *I*422).

Structure analysis. The geometry of NavAb structural models was assessed using PROCHECK[62]. The pore radius of NavAb was calculated using standard settings in the MOLE software[63]. Electrostatic surface calculations were performed with the APBS software[64], calculated with 150 mM NaCl in the solvent. Structural alignments were performed using LSQMAN[65] and O[61], where all channels were independently aligned onto NavAb based on the amino acid positions at the very beginning (that is, N-terminal portion) of their P-helices. The superposition of the atomic resolution Na^+-complex structure[40] shown in Supplementary Fig. 12 was positioned manually, but the K^+-channel and NaK-channel superpositions (Figs 2, 3, 5b and Supplementary Figs 12 and 13b) were obtained by simply aligning P-helices, as described earlier. All $F_o - F_c$ omit maps shown throughout the main text and Supplementary Information have been calculated using standard settings and appropriate buffers in the CNS program[60]. The $F_o - F_c$ omit map shown in Fig. 3b specifically derives from the 2.7 Å NaAb(Ile217Cys) data set and amino acids 170–183 were omitted from the calculation box. All structural figures were prepared with the PyMol software[66].

Electrophysiology. NavAb was cloned into the CDM8 vector and transfected into tsA-201 cells (along with a CD8 marker construct) using standard protocols. Whole-cell currents were recorded with continuous perfusion of extracellular solution using an Axopatch 200 amplifier (Molecular Devices) with glass pipettes polished to 2–4 MΩ resistance. The intracellular pipette solution contained (in mM): 10 NaCl, 105 CsF, 20 TEA, 10 EGTA, 10 HEPES pH 7.4 (adjusted with CsOH). The extracellular Na^+ solution contained (in mM): 100 NaCl, 1 $CaCl_2$, 1 $MgCl_2$, 1 KCl, 50 TEA, 10 HEPES pH 7.4 (CsOH). For K-containing and Cs-containing extracellular solutions, NaCl was replaced with KCl or CsCl, respectively. The extracellular NMDG solution contained (in mM): 100 NMDG, 1 $CaCl_2$, 1 $MgCl_2$, 1 KCl, 50 TEA, 10 HEPES pH 7.4 (HCl) and the extracellular Ca^{2+} solution contained (in mM): 75 $CaCl_2$, 1 $MgCl_2$, 1 KCl, 50 TEA, 10 HEPES pH 7.4 (CsOH). Voltage clamp pulses were generated and currents were recorded using Pulse software controlling an Instrutech ITC18 interface (HEKA). Data were analysed using Igor Pro 6.2 (WaveMetrics).

51. Koth, C. M. & Payandeh, J. Strategies for the cloning and expression of membrane proteins. *Adv. Protein Chem. Struct. Biol.* **76,** 43–86 (2009).
52. Cronin, C. N., Lim, K. B. & Rogers, J. Production of selenomethionyl-derivatized proteins in baculovirus-infected insect cells. *Protein Sci.* **16,** 2023–2029 (2007).
53. Chaptal, V. *et al.* Fluorescence Detection of Heavy Atom Labeling (FD-HAL): a rapid method for identifying covalently modified cysteine residues by phasing atoms. *J. Struct. Biol.* **171,** 82–87 (2010).
54. Faham, S. & Bowie, J. U. Bicelle crystallization: a new method for crystallizing membrane proteins yields a monomeric bacteriorhodopsin structure. *J. Mol. Biol.* **316,** 1–6 (2002).
55. Faham, S. *et al.* Crystallization of bacteriorhodopsin from bicelle formulations at room temperature. *Protein Sci.* **14,** 836–840 (2005).
56. Otwinowski, Z. & Minor, W. *Processing of X-ray Diffraction Data Collected in Oscillation Mode* Vol. 276 (Academic, 1997).
57. CCP4. The CCP4 suite: programs for protein crystallography. *Acta Crystallogr. D* **50,** 760–763 (1994).
58. Terwilliger, T. SOLVE and RESOLVE: automated structure solution and density modification. *Meth. Enzymol.* **374,** 22–37 (2003).
59. Adams, P. D. *et al.* PHENIX: a comprehensive Python-based system for macromolecular structure solution. *Acta Crystallogr. D* **66,** 213–221 (2010).
60. Brünger, A. T. *et al.* Crystallography & NMR system: a new software suite for macromolecular structure determination. *Acta Crystallogr. D* **54,** 905–921 (1998).
61. Jones, T. A., Zou, J. Y., Cowan, S. W. & Kjeldgaard, M. Improved methods for building protein models in electron density maps and the location of errors in these models. *Acta Crystallogr. A* **47,** 110–119 (1991).
62. Laskowski, R. A., Moss, D. S. & Thornton, J. M. Main-chain bond lengths and bond angles in protein structures. *J. Mol. Biol.* **231,** 1049–1067 (1993).
63. Petřek, M., Kosinova, P., Koca, J. & Otyepka, M. MOLE: a Voronoi diagram-based explorer of molecular channels, pores, and tunnels. *Structure* **15,** 1357–1363 (2007).
64. Baker, N. A., Sept, D., Joseph, S., Holst, M. J. & McCammon, J. A. Electrostatics of nanosystems: application to microtubules and the ribosome. *Proc. Natl Acad. Sci. USA* **98,** 10037–10041 (2001).
65. Kleywegt, G. J. Use of non-crystallographic symmetry in protein structure refinement. *Acta Crystallogr. D* **52,** 842–857 (1996).
66. DeLano, W. L. PyMOL molecular viewer (v. 1. 2r3pre) ⟨http://www.pymol.org⟩ (2002).